

A Unified Graph-based Framework for Scalable 3D Tree Reconstruction and Non-Destructive Biomass Estimation from Point Clouds

Di Wang^{a,b,*}, Shi Li^a

^aSchool of Software Engineering, Xi'an Jiaotong University, Xi'an 710049, China

^bShaanxi Joint (Key) Laboratory for Artificial Intelligence (Xi'an Jiaotong University), Xi'an 710049, China

Abstract

Estimating forest above-ground biomass (AGB) is crucial for assessing carbon storage and supporting sustainable forest management. Quantitative Structural Model (QSM) offers a non-destructive approach to AGB estimation through 3D tree structural reconstruction. However, current QSM methods face significant limitations, as they are primarily designed for individual trees, depend on high-quality point cloud data from terrestrial laser scanning (TLS), and also require multiple pre-processing steps that hinder scalability and practical deployment. This study presents a novel unified framework that enables end-to-end processing of large-scale point clouds using an innovative graph-based pipeline. The proposed approach seamlessly integrates tree segmentation, leaf-wood separation and 3D skeletal reconstruction through dedicated graph operations including *pathing* and *abstracting* for tree topology reasoning. Comprehensive validation was conducted on datasets with varying leaf conditions (leaf-on and leaf-off), spatial scales (tree- and plot-level), and data sources (TLS and UAV-based laser scanning, ULS). Experimental results demonstrate strong performance under challenging conditions, particularly in leaf-on scenarios (~20% relative error) and low-density ULS datasets with partial coverage (~30% relative error). These findings indicate that the proposed framework provides a robust and scalable solution for large-scale, non-destructive AGB estimation. It significantly reduces dependency on specialized pre-processing tools and establishes ULS as a viable alternative to TLS. To our knowledge, this is the first method capable of enabling seamless, end-to-end 3D tree reconstruction at operational scales. This advancement substantially improves the feasibility of QSM-based AGB estimation, paving the way for broader applications in forest inventory and climate change research.

Keywords:

LiDAR, Point Cloud, Graph, Tree Reconstruction, Above-ground Biomass, Quantitative Structure Model

1. Introduction

Trees play a crucial role in carbon sequestration, climate regulation, and biodiversity maintenance (Bonan, 2008), serving as primary carriers of carbon stocks in terrestrial ecosystems. Accurate estimation of Above-Ground Biomass (AGB) over large spatial extents is essential for evaluating forest carbon stocks and ecosystem service functions (Goetz et al., 2009). In particular, precise AGB assessments are not only vital for ecological research but also fundamental to the implementation and verification of global climate policies, such as the Paris Agreement and the Reducing Emissions from Deforestation and Forest Degradation (REDD+) program (Duncanson et al., 2019a). These initiatives rely on reliable carbon stock estimates to guide mitigation efforts and support carbon trading schemes.

The direct method of measuring AGB involves harvesting and weighing trees. However, this approach is not only harmful to the trees but also labor-intensive, time-consuming, and requires substantial manual effort along with strict quality control (Hyypä et al., 2001). Consequently, there is a growing

need for more efficient and scalable methods that enable accurate AGB estimation without extensive fieldwork and in a manner that minimizes damage to the trees. Remote sensing techniques have developed rapidly over the past decades, providing data with higher spatial resolution, finer spectral channels, and various modalities. These advancements make remote sensing increasingly useful for large-scale AGB estimations (Ometto et al., 2023). Nonetheless, remote sensing methods still require accurate ground data for developing, calibrating, and validating their biomass models and products (Labrière et al., 2023). In general, ground reference data typically rely on allometric models (Roxburgh et al., 2015). However, these models often necessitate calibration through destructive measures. Many allometric models are either inaccurate or unsuitable for specific geographical regions, constituting a major source of error in remote sensing AGB estimates (Chen et al., 2015).

Advances in Light Detection and Ranging (LiDAR) technology have provided a solid data foundation for tree structure analyses and biomass estimation (Calders et al., 2020). Due to its strong penetration capability and high spatial resolution, LiDAR is particularly effective at capturing the three-dimensional (3D) structural characteristics of trees, even in complex understory environments (Liang et al., 2016). A variety of LiDAR systems have been developed to address different for-

*Corresponding author

Email address: diwang@xjtu.edu.cn (Di Wang)

est mapping requirements. Terrestrial Laser Scanning (TLS) provides high-resolution, ground-based measurements that are ideal for detailed single-tree level structural analysis, while Airborne Laser Scanning (ALS) enables large-scale forest mapping, albeit with relatively lower point density. Mobile Laser Scanning (MLS) and UAV-based Laser Scanning (ULS) offer flexible deployment options for challenging terrains. Building upon these LiDAR-derived data sources, point cloud-based techniques have made significant progress across various aspects of tree structural analysis. These include the estimation of key tree parameters such as height, diameter at breast height (DBH), and crown dimensions (Wulder et al., 2012).

A particularly useful technique developed over the past decade is 3D tree reconstruction from point cloud data. The so-called tree Quantitative Structural Model (QSM) enables tree branching structure reconstruction and volume estimation in a non-destructive manner (Demol et al., 2022). Essentially, QSM is a 3D geometric and topological representation of a tree that captures its branching architecture with measurable attributes such as branch lengths, diameters, volumes, and spatial orientations (Ali et al., 2025). When combined with information on tree wood density, the QSM-estimated volume can be converted into AGB or even carbon storage, supporting a wide range of ecological and environmental studies (Calders et al., 2015). This approach provides an exciting and promising way to accurately estimate tree AGB without destructive measures. Numerous studies have demonstrated its superior performance compared to conventional allometric models, which require careful calibration (Calders et al., 2015; Momo Takoudjou et al., 2018; Gonzalez de Tanago et al., 2018).

However, despite significant progress in QSM techniques, several challenges continue to hinder its application in large-scale forest assessments. QSM typically operates on individual trees and requires single-tree point clouds as input. In practice, two prerequisite steps, individual tree segmentation and leaf-wood separation, must be performed prior to applying QSM at scale, and each of these steps can be technically challenging (Martin-Ducup et al., 2021b). Second, current QSM methods generally require high-density and well-covered point cloud data. As a result, multi-scan TLS data are most commonly used (Demol et al., 2022). However, acquiring large-scale TLS data can be labor-intensive and time-consuming, particularly in complex or difficult-to-access terrain (Ye et al., 2019). Lastly, many existing approaches rely on complex, manually tuned workflows that are not easily transferable across diverse or multi-source datasets (Zhang et al., 2023). Collectively, these limitations constrain the scalability and practical applicability of QSM-based biomass estimation in real-world forest monitoring scenarios.

In this study, we propose a unified 3D tree reconstruction framework based on graph processing, designed to enable scalable and fully automated 3D tree reconstruction from large-scale point cloud data, with a primary focus on its application to non-destructive AGB estimation. The core idea involves transforming point cloud data into a graph-based representation, followed by a series of graph operations to perform key tasks such as individual tree segmentation, leaf-wood separa-

tion, and 3D skeletal reconstruction. This novel framework demonstrates strong robustness to variations in point cloud density and foliage conditions, achieving reliable performance even on sparse ULS data. We evaluate the effectiveness of the framework across various data acquisition settings and discuss its potential for enabling efficient, large-scale, and automated AGB estimation in diverse environments.

2. Related Work

2.1. QSM Methods

Over the past decade, QSM-based methods have made substantial progress in AGB estimation by enabling non-destructive and geometry-informed tree volume modeling. Demol et al. (2022) provides a comprehensive overview of QSM-based AGB studies, revealing that QSM-derived estimates closely agree with destructive measurements (bias <1%, concordance correlation coefficient of 98%). However, performance tends to be lower for smaller trees and conifer species. Despite these limitations, QSM-based methods are consistently less biased and more accurate than allometric scaling models (ASMs), particularly for larger trees. With such capabilities, QSM-based AGB estimation is regarded as a revolutionary technique that advances forest structure analysis and carbon monitoring (Duncanson et al., 2021).

Driven by these advantages, QSM methods have rapidly evolved over the past decade. Existing QSM approaches can generally be divided into two main categories, segmentation-based and skeleton-based methods. Segmentation-based methods reconstruct tree geometry by partitioning the point cloud into local segments, each of which is typically fitted with a geometric primitive such as a cylinder. TreeQSM, proposed by Raunonen et al. (2013), is among the most widely used QSM tools. It adopts a bottom-up strategy to construct tree topology and fits segmented point clouds with cylindrical models to achieve 3D reconstruction. Around the same time, Pype-Tree was introduced as another influential method (Delagrangue et al., 2014). This approach reconstructs tree architecture by fitting branching geometries through recursive decomposition of the point cloud. Later, Hackenberg et al. (2015) proposed the SimpleTree method, which simplifies the modeling process by allowing users to generate cylindrical structures based on pre-defined parameters.

In contrast, skeleton-based methods directly extract the skeleton from the input point cloud. Mei et al. (2017) proposed a method in which tree skeletons are extracted by utilizing the L1-median skeleton followed by a data completion scheme that guides the compensation for missing data. Du et al. (2019) proposed the AdTree model which uses a minimum spanning tree (MST) to extract an initial skeleton and applies iterative simplification to reconstruct tree morphology. This method was later improved for tree structural analyses in AdQSM (Fan et al., 2020). Li et al. (2020) introduced an improved Laplacian-based contraction algorithm to extract detailed branch architecture attributes from TLS data achieving high accuracy in estimating branch angles and diameters. Li et al. (2022) split the

point cloud into main thick and small branches then applied graph shortest path analysis to generate the skeleton. More recently Feng et al. (2024a) proposed L1-Tree which leverages L1-median geometry combined with structural optimization to enhance topological accuracy especially in sparse or noisy TLS point clouds.

It should be noted that most QSM methods are designed for leaf-off point clouds, as the presence of leaf points can lead to inaccurate delineation of tree branching structures, often causes overestimation of tree volume and AGB (Demol et al., 2022). This issue is particularly relevant for segmentation-based methods, as they directly fit geometric primitives to point data. In general, a leaf-wood separation step is recommended to filter out leaf points (Wang et al., 2020). A recent study by Chen et al. (2025) systematically evaluated the influence of leaf-wood separation algorithms on subsequent QSM-based AGB estimations. The results showed that leaf-removed AGB estimates tend to underestimate the true values for both coniferous and broadleaved trees, although the underestimation is generally less pronounced in broadleaved species.

Overall, QSM methods are rapidly evolving. There is a growing emphasis on improving robustness to data occlusion and adaptability to heterogeneous scanning conditions.

2.2. Large-Scale Tree 3D Reconstruction

Despite the rapid development of QSM methods, most of these approaches are designed for reconstructing individual trees. Extending QSM to larger scales, such as plot-level applications, has remained a key area of interest.

Since existing QSM methods operate at the single-tree level, a prerequisite for plot-scale application is the accurate segmentation of individual trees from large-scale point cloud data. Raunonen et al. (2015) proposed a morphology-based approach for individual tree modeling using cover set-based trunk detection. After segmenting individual trees, TreeQSM was applied to reconstruct each tree’s structure. However, its applicability is largely limited to forest plots with sparse tree distributions, where individual tree structures can be more easily distinguished (Burt et al., 2019). Martin-Ducup et al. (2021b) evaluated automated QSM pipelines in a 1-hectare tropical forest plot and emphasized that effective tree segmentation remains a critical challenge for scaling up AGB estimation. Fan et al. (2022) proposed a clustering-based method to group individual trees before applying AdQSM for 3D reconstruction. Their results showed that the relative bias in total AGB estimation was less than 20% using this workflow. In general, current large-scale QSM applications all rely on separate tree segmentation algorithms as a preprocessing step. This dependency introduces additional complexity, especially in dense or structurally complex forests.

In addition, an important factor influencing the scalability of QSM is data acquisition efficiency. Most current QSM methods are based on TLS data, which is widely regarded as the benchmark for high-resolution structural reconstruction of individual trees (Duncanson et al., 2019b). However, large-scale TLS campaigns are labor- and time-intensive, limiting their feasibility for extensive forest monitoring (Wilkes et al., 2023). As

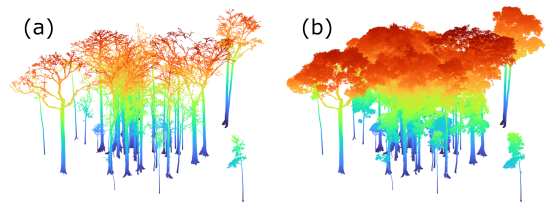


Figure 1: Visualization of TLS data of 61 tropical trees under (a) leaf-off and (b) leaf-on conditions.

a result, researchers have started to explore more efficient data acquisition strategies for large-scale QSM applications, such as MLS and ULS. Ye et al. (2019) constructed QSM models using ULS point clouds but noted that severe occlusion and structural incompleteness significantly hindered the accuracy of AGB estimation. Similarly, Brede et al. (2022) applied QSM to ULS data for tree volume estimation and found that model performance declined in denser stands and for trees with finer branching structures. To address these limitations, Terryn et al. (2022) explored the integration of TLS and ULS data to extract tree structural parameters. Instead, Vandendaele et al. (2024) used MLS data to reconstruct individual trees in a 1-hectare temperate hardwood stand using TreeQSM, demonstrating the potential of MLS for accurate and non-destructive estimation of tree structural attributes. Furthermore, Reckziegel et al. (2025) reported no statistically significant differences between ULS and TLS-derived estimates of tree height, canopy cover, diameter, and wood volume in open savanna systems. However, the applicability of such findings remains questionable under conditions of higher canopy closure or in structurally complex understory environments.

Overall, there is growing interest in applying QSM for large-scale AGB estimation. Leveraging more data-efficient platforms such as MLS and UAS-LiDAR holds great potential for advancing applications from plot to landscape scales. However, most current QSM workflows still rely on separate single-tree segmentation and leaf-wood separation algorithms, which limits their scalability. Moreover, the generally lower data quality from MLS and ULS compared to TLS poses additional challenges to the robustness of QSM methods, as highlighted by previous studies (Brede et al., 2022).

3. Datasets

To comprehensively evaluate the effectiveness of the proposed framework, we curated four distinct datasets spanning a range of data scales (individual trees and plot), leaf conditions (leaf-off and leaf-on states), and LiDAR platforms (TLS and ULS). A detailed description of each data set is provided in the following. Table 1 summarizes the key characteristics of these datasets.

3.1. Tree-scale Leaf-off TLS Data

For individual tree-scale analysis, this study utilized data from Momo Takoudjou et al. (2018). The dataset includes 61 tropical trees located in the semi-deciduous forests of eastern

Table 1: Statistics of the compiled datasets. An asterisk (*) denotes the algorithm-estimated total number of trees within the provided point clouds, while numbers in parentheses indicate the actual number of trees used in this study.

| Data | Leaf Condition | Location | Biome | Number of Trees | DBH (cm) | Height (m) |
|----------------|----------------|-----------|---------------------|-----------------|-------------|--------------|
| Tree-scale TLS | Off | Cameroon | Tropical Rainforest | 61 | 58.37±41.3 | 33.72 ±12.41 |
| Tree-scale TLS | On | Cameroon | Tropical Rainforest | 61 | 58.37±41.3 | 33.72 ±12.41 |
| Plot-scale TLS | On | Australia | Temperate Forest | 270* (34) | 34.68±14.72 | 18.61 ± 4.61 |
| Tree-scale ULS | On | Germany | Temperate Forest | 2419* (29) | 41.67±19.22 | 27.31±4.74 |

Cameroon (4°02'20.77"N, 14°55'49.15"E), near Lobéké National Park. These trees represent 15 different species, with a mean DBH of 58.37 cm (± 41.30) and a mean height of 33.72 m (± 12.41) (Table 1). The maximum stem diameter measured along any part of the tree reached up to 186.6 cm. All trees were destructively sampled to obtain ground-truth biomass measurements, providing a unique benchmark for evaluating biomass estimation methods, particularly for structurally complex tropical trees.

TLS data were collected using a Leica C10 ScanStation (Leica Geosystems), a time-of-flight laser scanner operating at a 532 nm wavelength. Each tree was scanned from at least three positions to ensure unobstructed views and comprehensive coverage. The acquired TLS point clouds included leaf points, which were manually removed by the original authors to facilitate accurate 3D model reconstruction (Figure 1a). For further details on data acquisition and processing, refer to Momo Takoudjou et al. (2018).

This dataset serves as a critical benchmark for validating the core performance of our method in estimating individual tree biomass, a fundamental capability expected of any 3D reconstruction-based biomass estimation approach. We selected this unique data set because the tropical trees involved represent some of the most challenging conditions for 3D tree reconstruction, due to their large crown sizes and structural complexity (Gonzalez de Tanago et al., 2018).

3.2. Tree-scale Leaf-on TLS Data

The same dataset described in Section 3.1, but acquired under leaf-on conditions (Figure 1b), is used to evaluate the performance of our method in the presence of foliage. One of the distinctive capabilities of our approach is its intrinsic ability to mitigate the impact of leaf points through the specifically designed graph-based framework. Therefore, the results obtained from the leaf-on data are analyzed to provide insight into the robustness of our method when processing leaf-on point clouds. This also enables a cross-comparison with results from leaf-off TLS data, offering deeper understanding of the influence of leaf points on AGB estimation.

3.3. Plot-scale TLS Data

Plot-scale TLS data were provided by Calders et al. (2015), collected from a native Eucalypt Open Forest in Victoria, Australia (Figure 2). The study plot, named RUSH06, has a side length of 50 m, with a stem density of 347 stems per hectare and a basal area of 13 m² per hectare.

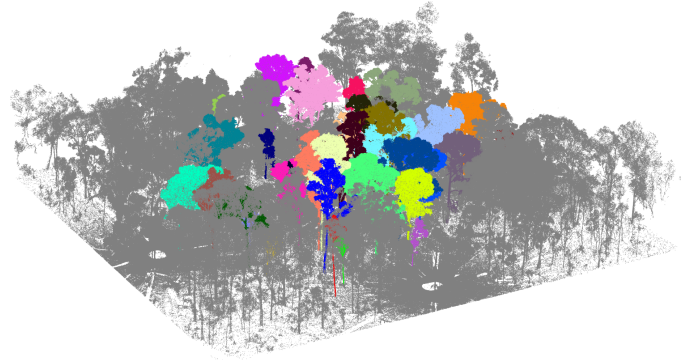


Figure 2: Visualization of the TLS point cloud for the RUSH06 plot. The 34 destructively sampled trees are highlighted with random coloring to distinguish individual trees.

A subset of 34 destructively sampled trees from the RUSH06 plot was used in this study. These trees represent three dominant species, including *Eucalyptus leucoxylon*, *Eucalyptus microcarpa*, and *Eucalyptus tricarpa*. They were harvested to obtain reference AGB values. Fresh weights (FW) were measured in the field using a digital crane scale. For each species, stem discs were collected every 3 meters along the trunk of a representative tree, oven-dried at 70°C to determine dry weight (DW), and species-specific DW:FW ratios were calculated. These ratios were then applied to convert total fresh biomass into dry biomass.

TLS data were acquired using a RIEGL VZ-400 scanner (RIEGL Laser Measurement Systems GmbH), with five scan positions per plot (one at the center and four located at 40 m from the center). An additional tilted scan was performed at each location to capture the full hemisphere. Point clouds were registered using RiSCAN PRO software, resulting in an average registration error of 0.0129 m. The individual tree point clouds from 34 destructively sampled trees, made available by the authors, are used in this study as reference data for validation purposes. Terrain points were removed in advance using the method of Zhang et al. (2016).

3.4. ULS Data

ULS data are included in this study to specifically evaluate the robustness of our method for sparse and partially covered point clouds. This is particularly relevant as ULS data are increasingly favored in large-scale analyses. The dataset was derived from the study by Weiser et al. (2022), conducted in the Bretten municipal forest in Baden-Württemberg, Germany. The study site is a temperate mixed forest located in a hilly landscape, with dominant tree species including European beech,

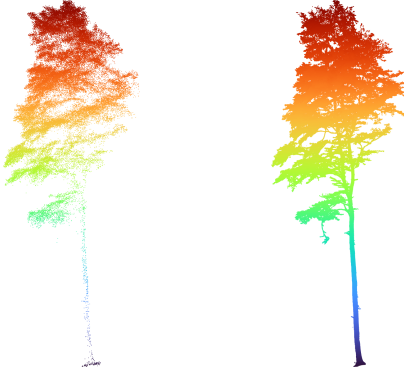


Figure 3: Visualization of ULS (left) and corresponding TLS (right) data for an example tree.

Douglas fir, spruce, and various oak species. The forest consists of multi-layered, mixed-species stands characterized by dense canopy cover.

ULS data were collected using a RIEGL miniVUX-1UAV sensor (RIEGL Laser Measurement Systems GmbH), mounted on a DJI Matrice 600 Pro UAV during multiple flight campaigns between 2019 and 2020. A double-grid flight pattern was employed to ensure full coverage. Point cloud data were post-processed using RiPROCESS software and aligned with GNSS reference data. Filtering steps were applied to remove outliers and off-nadir noise. Co-registered TLS data were acquired using a RIEGL VZ-400 terrestrial laser scanner in 2019. Multiple scan positions (typically 5–8 per plot) were arranged around groups of trees to ensure comprehensive coverage. Reflective cylindrical targets were used for initial registration, followed by multi-scan adjustment and alignment with the ULS data using iterative closest point (ICP) algorithms.

The original dataset contains manually segmented paired ULS and TLS data for 29 individual trees (Figure 3). This provides a unique opportunity to evaluate the robustness of our method under conditions of significantly reduced point density and incomplete coverage with ULS data. Since this dataset does not include destructively measured AGB data, we cross-validate the ULS-derived results against TLS-derived estimates, assuming TLS as the reference due to its well-established accuracy in biomass estimation (Brede et al., 2022).

4. Methodology

The core idea of our method is to transform the point cloud into a graph representation, on which all subsequent processing steps are then performed. Figure 4 shows the overall workflow. We first achieve individual tree segmentation through a *graph pathing* step that splits the original graph into multiple subgraphs, with each subgraph corresponding to a single tree’s point cloud. Subsequently, for each subgraph (i.e., individual tree), we introduce a step termed *graph abstracting*, which directly extracts a 3D skeleton graph representing the tree topological structure. This skeleton graph, together with the radius information at each skeleton node, constitutes a 3D tree model.

In the following sections, we provide detailed descriptions of each of these steps.

4.1. Graph Construction

We represent the original point cloud as an undirected graph $G = (V, E, W)$, where $V = \{v_1, v_2, \dots, v_n\}$ denotes the set of nodes. Each node $v_i \in V$ corresponds to a point in the original point cloud, and the edge set E contains undirected edges e_{ij} that connect certain pairs of neighboring points. The weight function W assigns a weight to each edge in E . The weight w_{ij} of an edge e_{ij} is defined as the Euclidean distance between the two nodes v_i and v_j constituting the edge.

The graph G is a hybrid graph constructed based on both the k -nearest neighbors (KNN) and Delaunay triangulation algorithms to connect nodes (Wang et al., 2021). First, a KNN graph (with $k = 10$) is built using the KD-tree structure. Subsequently, the graph is pruned to remove dispersed edges. Specifically, for each node, any edge whose length deviates by more than one standard deviation from the average length of its connected edges is removed. This process enables local pruning and optimization of the graph. Next, Delaunay triangulation is applied to generate a fully connected graph Du et al. (2019). The Delaunay edges are sorted in ascending order of their lengths. These edges are then progressively added to the previously pruned KNN graph until the resulting graph becomes fully connected, forming a single connected component. This strategy ensures both local and global connectivity of the final graph while avoiding redundant and overly long edges that could disrupt local connectivity. A similar approach has also been adopted in previous studies on tree point cloud segmentation (Wang et al., 2021).

4.2. Graph Pathing - Single Tree Extraction

Our previous work, *graph pathing*, is applied to the graph G to extract individual trees (Wang et al., 2021). The key idea of graph pathing is to allow each node (i.e., point) in the graph to traverse towards its lowest reachable node, which can be considered as its root node. This procedure mimics the reverse transport of water and nutrients in trees, from the branches back to the roots (Tao et al., 2015). Despite its conceptual simplicity, this approach has demonstrated excellent performance and high computational efficiency. Moreover, it accurately segments understory vegetation that is not part of tree structures. A full description of the graph pathing step can be found in Wang et al. (2021).

The outcome of *graph pathing* is a set of subgraphs $H_i = (V_i, E_i, W_i)$ of the original graph G , where each subgraph represents an individual tree. Specifically, the points corresponding to each node in H_i constitute the point cloud of a single tree (Figure 4). Formally, the partitioning satisfies:

$$\bigcup_{i=1}^k V_i = V, \quad \bigcap_{i=1}^k V_i = \emptyset, \quad \text{and} \quad \bigcup_{i=1}^k E_i \subseteq E.$$

Since the extracted subgraphs may no longer guarantee full connectivity, we apply the same Delaunay triangulation strategy introduced in Section 4.1 to repair H when necessary.

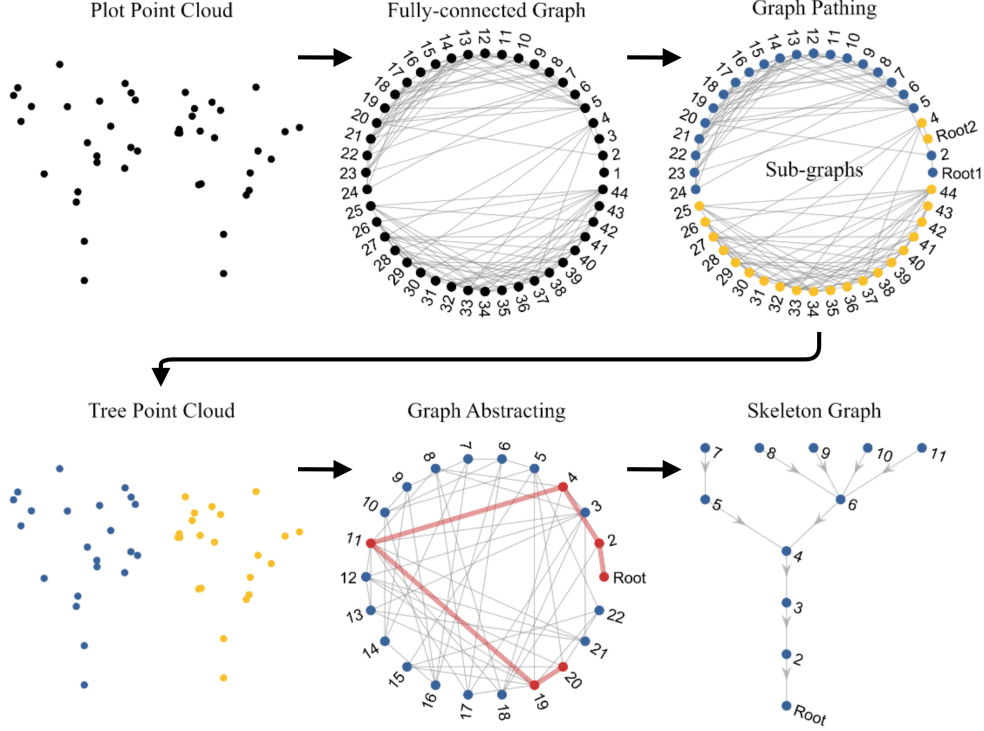


Figure 4: Workflow of the proposed graph-based framework.

4.3. Graph Abstracting - 3D Skeleton Extraction

For each subgraph $H_i = (V_i, E_i, W_i)$ obtained from the previous *graph pathing* step, we propose a *graph abstracting* step to further extract the 3D skeleton of individual trees.

Similar to many graph-based skeleton extraction methods (Mei et al., 2017; Du et al., 2019), our approach first applies Dijkstra’s shortest path algorithm to compute the shortest paths P_{th} from each node to the root node. Collectively, these paths represent the overall structure of the tree. However, they are highly redundant, as each branch contains a large number of points, and each point has an individual path. Ideally, each branch should be represented by a single path, corresponding to the skeleton. Therefore, the key step is to simplify the graph structure. While existing methods often rely on techniques such as MST or its simplification variants (Du et al., 2019), we instead apply a simple adaptive clustering method to draw the tree skeleton.

4.3.1. Node Metrics

The shortest path analysis yields, for each node $v_i \in \mathcal{V}$, two key attributes, the shortest path $\mathcal{P}_{th}(v_i)$ from v_i to its root $r(v_i)$, and the corresponding distance $D_i = \sum_{e \in \mathcal{P}_{th}(v_i)} W(e)$. Based on this, we propose two metrics to characterize structural properties, *path frequency* \mathcal{F} and *farthest tip* \mathcal{T} .

Path Frequency \mathcal{F} . The path frequency \mathcal{F}_i of a node v_i quantifies its topological importance by counting how often it appears in all shortest paths \mathcal{P} in the graph:

$$\mathcal{F}_i = |\{P \in \mathcal{P} \mid v_i \in P\}|,$$

where \mathcal{P} denotes the set of all shortest paths in H_i . This metric was originally introduced by Vicari et al. (2019) to capture hierarchical structures in tree-like graphs. However, due to sparse coverage in shortest paths, some nodes may remain unvisited ($\mathcal{F}_i = 0$). To resolve this, we refine \mathcal{F}_i using a propagation correction:

$$\mathcal{F}'_i = \begin{cases} \max\left(\mathcal{F}_i, \max_{\substack{v_j \in \mathcal{N}(v_i) \\ D_j < D_i}} \mathcal{F}'_j\right), & \text{if } \mathcal{F}_i < \max_{\substack{v_j \in \mathcal{N}(v_i) \\ D_j < D_i}} \mathcal{F}'_j, \\ \mathcal{F}_i, & \text{otherwise.} \end{cases}$$

where $\mathcal{N}(v_i)$ is the set of neighbors of v_i , and D_j is the root distance of node v_j . This means that for a node v_i , if its \mathcal{F}_i value is smaller than that of any node directly connected to it with a smaller distance D , then \mathcal{F}_i is updated to match the maximum \mathcal{F} value among those nodes. This correction ensures monotonicity in \mathcal{F} values along the hierarchy defined by D , eliminating discontinuities. Visualization of the path frequency \mathcal{F} is shown in Figure 5b.

Farthest Tip \mathcal{T} . In contrast, the farthest tip \mathcal{T} identifies the terminal (tip) node that is farthest from the root along the path traced by a given node. For instance, for a node v_i , its corresponding farthest tip is defined as the terminal node with the maximum farthest distance to the root that can be reached via v_i along the shortest path. Formally, the farthest tip \mathcal{T}_i of a node v_i is defined as the terminal node $t \in V$ satisfying:

$$\mathcal{T}_i = \arg \max_{t \in \mathcal{T}} (D_t \mid \exists P \in \mathcal{P}(v_i, t)),$$

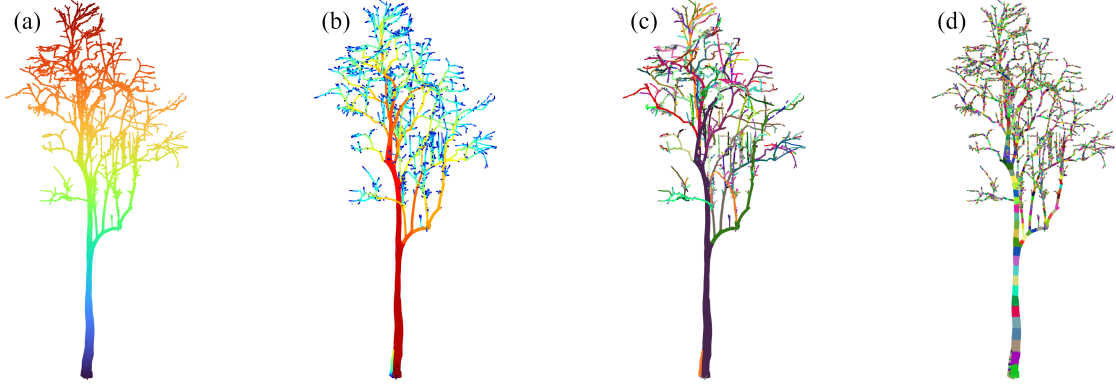


Figure 5: (a) Point cloud of an example tree. (b) The point cloud colored according to the path frequency \mathcal{F} in log scale, ranging from light blue (low values) to dark red (high values). (c) Visualization based on the farthest tip \mathcal{T} metric, where points belonging to the farthest tip are assigned the same color. (d) Result of adaptive clustering applied to the point cloud, with each cluster represented by a distinct random color.

where $\mathcal{T} = \{v \in \mathcal{V} \mid \text{out-degree}(v) = 0\}$ is the set of terminal nodes, and $\mathcal{P}(v_i, t)$ is the set of paths from v_i to t . After computing \mathcal{T}_i , similar to \mathcal{F} , we apply the propagation correction:

$$\mathcal{T}'_i = \begin{cases} \arg \max_{\substack{v_j \in \mathcal{N}(v_i) \\ D_j < D_i}} (D_{\mathcal{T}'_j}), & \text{if } D_{\mathcal{T}_i} < \max_{\substack{v_j \in \mathcal{N}(v_i) \\ D_j < D_i}} D_{\mathcal{T}'_j}, \\ \mathcal{T}_i, & \text{otherwise.} \end{cases}$$

Here, $D_{\mathcal{T}_i}$ denotes the distance of the tip node \mathcal{T}_i to the root. This correction ensures that the farthest tip \mathcal{T}'_i reflects the globally farthest tip within the subtree rooted at v_i , even if \mathcal{T}_i is not the absolute maximum. We find that the metric \mathcal{T} is particularly effective in delineating individual branches, as all nodes belonging to the same branch share the same farthest tip node (Figure 5c). This naturally provides a segmentation that divides the point cloud into distinct branches.

Consequently, these two metrics provide a robust foundation for the *graph abstracting* step. \mathcal{F} reveals the topological hierarchy, enabling the identification of the skeleton structure, while \mathcal{T} facilitates the decomposition of points into distinct clusters, from which the skeleton nodes can be directly derived.

4.3.2. Skeleton Extraction

Adaptive Clustering. Based on the farthest tip assignment \mathcal{T}'_i , the point cloud of a single tree can be naturally partitioned into disjoint clusters, where each cluster corresponds to a distinct branch:

$$\mathcal{B}_t = \{v_i \in \mathcal{V} \mid \mathcal{T}'_i = t\}, \quad \forall t \in \mathcal{T}.$$

This segmentation is visualized in Figure 5c, where nodes sharing the same terminal tip are grouped together.

To further subdivide each branch into finer hierarchical segments (e.g., for skeletonization), one may consider segmenting based on root distance D_i using a fixed step size d_s , as done in prior work (Fu et al., 2020). However, this approach exhibits major limitations. A large d_s results in an overly coarse skeleton, failing to capture fine crown structures. While a small d_s generates excessive redundancy, especially along trunk segments with minimal topological variation.

To overcome these limitations, we introduce a reverse distance metric $D_T(v_i)$, defined as the shortest path distance from node v_i to its corrected farthest tip \mathcal{T}'_i :

$$D_T(v_i) = D_{\mathcal{T}'_i} - D_i,$$

where $D_{\mathcal{T}'_i}$ denotes the root distance of the corrected tip node \mathcal{T}'_i . Using D_T , we define a non-uniform step size function $d_s(D_T)$ that adapts dynamically to local structure. Given the reverse distance metric D_T , we define the non-uniform step size vector \mathbf{d}_s as:

$$\mathbf{d}_s = \frac{D_{\mathcal{T}'_{\max}} - D_{\mathcal{T}'_{\min}}}{\alpha} \cdot \left(10^{(\text{linspace}(0, \log_{10}(\alpha+1), 100))} - 1\right) + D_{\mathcal{T}'_{\min}}.$$

The parameter α controls the exponential behavior and is set to 20 in this study. This strategy ensures fine sampling near $D_T(v_i) = 0$ (crown regions) and coarse sampling near $D_T(v_i) = D_{\mathcal{T}'_{\max}}$ (trunk regions), yielding a compact yet expressive skeletal representation. The resulting segmentation is shown in Figure 5d.

It should be noted that, in leaf-on point clouds, the farthest tip \mathcal{T} often fails to accurately distinguish individual branches. This is primarily due to the dense packing of leaf points, which obscures clear separations between adjacent branches. To address this issue, we further apply a mean-shift clustering step (Comaniciu and Meer, 1999). The bandwidth parameter of the mean-shift algorithm is set to match the non-uniform step size d_s , thereby maintaining an adaptive strategy. This allows for finer clustering of points in branch tip regions, enhancing the overall resolution of the branching structure.

Skeleton Graph. With the adaptive clustering in place, we extract a single representative node from each cluster. Specifically, the node with the highest path frequency \mathcal{F} is selected. To improve spatial accuracy, we then adjust the position of each selected node to the L1-median of its corresponding cluster (Feng et al., 2024b). This step ensures that the skeleton node is located at the central axis of the branch, thereby enhancing the geometric fidelity of the resulting tree model. These extracted nodes serve as the skeleton nodes, effectively capturing the overall structure of the tree (Figure 6).

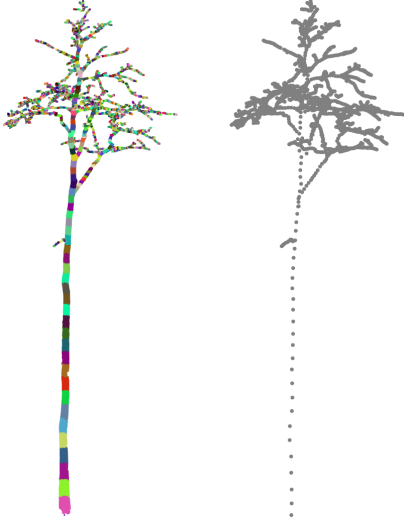


Figure 6: Adaptive clustering of a tree point cloud and its corresponding skeleton points. It also demonstrates that our method preserves fine structural details within the crown while avoiding redundant segmentation in the trunk region.

The next step involves connecting these skeleton nodes to form a directed graph, representing the tree’s structural skeleton. Since the shortest path $\mathcal{P}_{\text{th}}(v_i)$ for each node is already known, this information can be naturally aggregated to the cluster level, resulting in a corresponding cluster shortest path $\mathcal{P}_{\text{th}}(\mathcal{B})$. As a result, we obtain the shortest path from each cluster to the root cluster (i.e., the one containing the root node). This means there is no need to recompute the skeleton graph from scratch. Instead, it can be directly abstracted from the existing graph. This is why we refer to this process as *graph abstracting*.

4.3.3. Controlling Skeleton Granularity - Impact of Leaf Points

Each extracted skeleton node is associated with a corresponding path frequency value \mathcal{F}_i . As discussed in Section 4.3.1, the path frequency \mathcal{F} effectively captures the topological hierarchy inherent in tree-like branching structures. An example is illustrated in Figure 7. Since leaves grow at the extremities of branches, the skeleton nodes representing leaf positions typically exhibit very low \mathcal{F} values. This property allows us to control the granularity of the reconstructed tree skeleton by simply applying a threshold on \mathcal{F} , enabling flexible simplification or refinement of the structure as needed.

Figure 8 demonstrates that this simple strategy effectively controls the granularity of the resulting tree skeletons (i.e., 3D models). By gradually increasing the minimum threshold of the \mathcal{F} value, the tree models retain only the main structural components while progressively filtering out leaf nodes and finer branches. This capability is particularly valuable for AGB estimation from leaf-on point clouds, as it eliminates the need for a separate leaf removal step. The proposed framework thus provides an elegant, unified solution that seamlessly integrates single-tree extraction, leaf-wood separation, and 3D skeleton reconstruction into a cohesive processing pipeline.

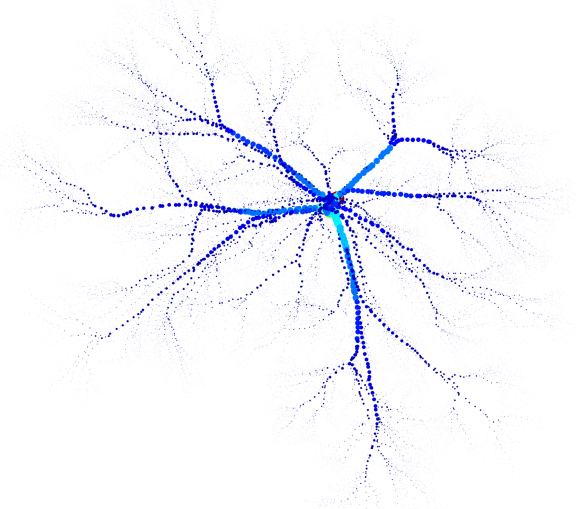


Figure 7: Top view of the skeleton points of a tree. Each point is scaled and colored according to its path frequency value: darker blue indicates lower values, and lighter blue indicates higher values. Point size increases with increasing path frequency.

4.4. Skeleton to 3D Tree Model

Tree 3D skeletons are further transformed into geometric models using generalized cylinders. Following established practices in graph-based tree 3D reconstruction (Du et al., 2019; Fu et al., 2020), we apply allometric scaling principles to estimate the branch radius at each node within the skeleton (West et al., 1999). Specifically, the relationship between the radius of a parent node and its child node is governed by the following equation:

$$R_c = R_p \cdot \left(\frac{l_c}{l_p}\right)^\gamma, \quad (1)$$

where R_c denotes the radius at the child node, R_p is the radius of the parent node, l_c and l_p represent the total lengths of the subtrees supported by the child and parent nodes, respectively, and γ is a scaling exponent. Empirical studies suggest setting $\gamma = 1.5$ when a parent node has a single child, and $\gamma = 0.4$ when it has multiple children (West et al., 1999).

Once the skeleton and corresponding radii are determined, we proceed to construct the 3D geometric model. We employ cubic Hermite splines to smooth each branch skeleton, following which generalized cylinders are used to define the surface geometry of each branch (Hu et al., 2017). This approach enables the generation of a comprehensive and complete 3D geometric tree model.

4.5. Evaluation Metrics

Since we target AGB estimation from reconstructed 3D tree models, two widely used metrics, the Mean Absolute Deviation (MAD) and the Mean Absolute Percentage Deviation (MAPD), were employed to compare the estimated biomass with the reference values Ali et al. (2025). MAD quantifies the average magnitude of the absolute differences between the algorithm-estimated biomass (Biomass_a) and the destructively

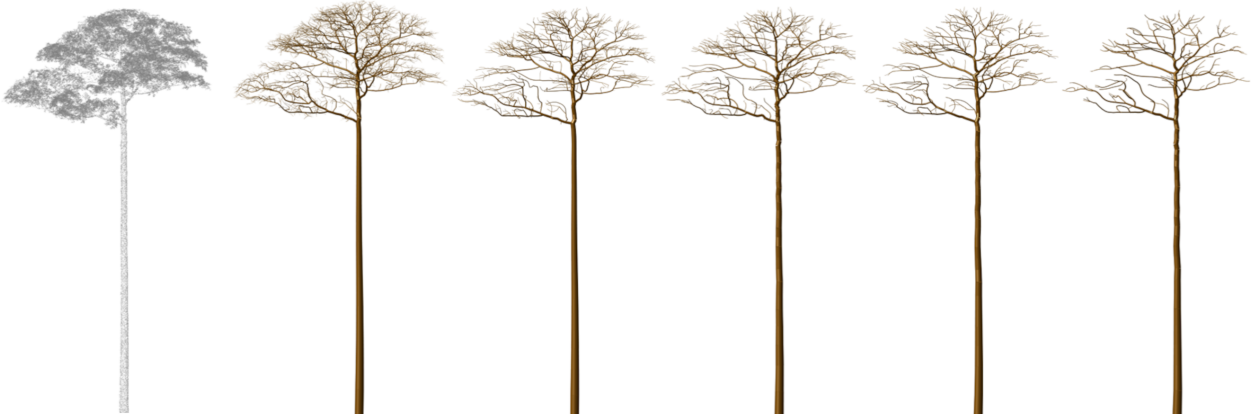


Figure 8: Point cloud of a tree and its corresponding reconstructed 3D tree models using different path frequency \mathcal{F} thresholding. From left to right: increasingly higher minimum thresholds of \mathcal{F} are applied, retaining only the main branches as the less significant structures are filtered out.

measured reference biomass (Biomass_d), as defined in Equation 2. MAPD, expressed as a percentage, provides a relative measure of these deviations with respect to the reference biomass. This allows for meaningful performance comparisons across datasets with varying tree sizes, as detailed in Equation 3.

$$MAD = \frac{1}{n} \sum_{i=1}^n |\text{Biomass}_{.a_i} - \text{Biomass}_{.d_i}| \quad (2)$$

$$MAPD = \frac{100\%}{n} \sum_{i=1}^n \left| \frac{\text{Biomass}_{.a_i} - \text{Biomass}_{.d_i}}{\text{Biomass}_{.d_i}} \right| \quad (3)$$

Here, n represents the total number of trees in the dataset, and i denotes the individual tree index. These metrics provide a comprehensive view of the algorithm performance, balancing absolute and relative error assessments, and enable standardized comparisons between different reconstruction approaches.

4.6. Methods Comparison

We compare our method with two established and widely used QSM approaches, TreeQSM (Raumonen et al., 2013) and AdQSM (Fan et al., 2020), for tree-level AGB estimation. Both methods are designed for individual trees, making them suitable for comparison at the tree scale. TreeQSM is often considered a standard QSM method for AGB estimation due to its accuracy and reliability (Demol et al., 2022). AdQSM, on the other hand, is also a graph-based 3D tree reconstruction method that shares a similar conceptual framework with our approach, although it is limited to single-tree applications. We use the latest implementations of both methods, which are publicly available at their respective GitHub repositories. Default parameter settings are employed for both methods. For TreeQSM, this involves performing multiple runs with different parameter combinations to automatically select the optimal model (Ali et al., 2025).

The comparisons were conducted using both leaf-on and leaf-off TLS data at the tree scale. For plot-scale TLS data, we focus on detailed analyses of the impact of individual tree segmentation. In the case of ULS data, we cross-compare the

Table 2: Results of AGB estimation on single-tree scale TLS data.

| Methods | Leaf Condition | MAD (Mg) | MAPD (%) |
|---------|----------------|----------|----------|
| Ours | Off | 1.78 | 17.05 |
| | On | 1.15 | 21.53 |
| TreeQSM | Off | 0.78 | 10.99 |
| | On | 6.76 | 169.34 |
| AdQSM | Off | 3.29 | 35.03 |
| | On | 6.61 | 50.18 |

results from TLS and ULS to evaluate the effectiveness of our method in reconstructing branching structures from low-density ULS point clouds.

5. Results

5.1. Tree-scale TLS Data

5.1.1. Leaf-off Condition

Table 2 summarizes the results of AGB estimation on both leaf-off and leaf-on TLS data. For the leaf-off dataset, TreeQSM achieved the best accuracy with a MAPD of 10.99%, followed by our method at 17.05%, while AdQSM showed the highest MAPD of 35.05%.

Figure 9 further illustrates the AGB estimation results, demonstrating that our method generally agrees well with the reference values, achieving an R^2 of 0.93 and a slightly overall overestimation. The strong performance of TreeQSM (e.g., R^2 of 0.97) is consistent with findings from recent studies using the same dataset (Ali et al., 2025).

5.1.2. Leaf-on Condition

For the leaf-on condition, our method demonstrated strong consistency by achieving a MAPD of 21.53%, whereas both TreeQSM and AdQSM performed worse compared to the leaf-off condition (Table 2). In particular, TreeQSM showed a significant increase in MAPD, reaching 169.34%. Figure 10 illustrates that both TreeQSM and AdQSM substantially overestimated AGB under the leaf-on condition. This is expected, as the presence of leaves has a considerable impact on 3D tree

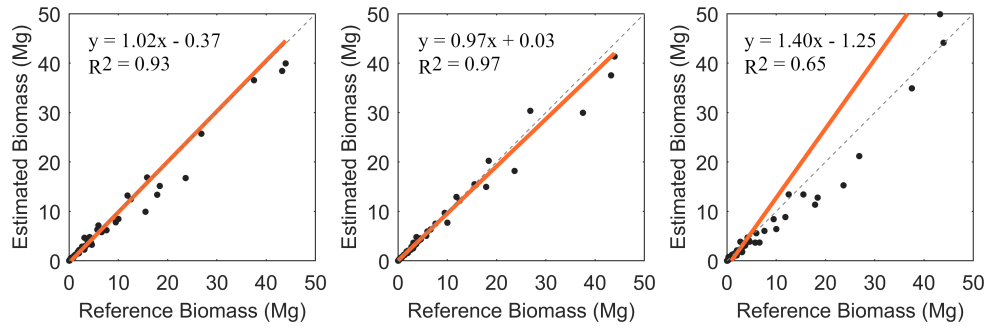


Figure 9: Left to right: Results of AGB estimation on leaf-off TLS data using our method, TreeQSM, and AdQSM.

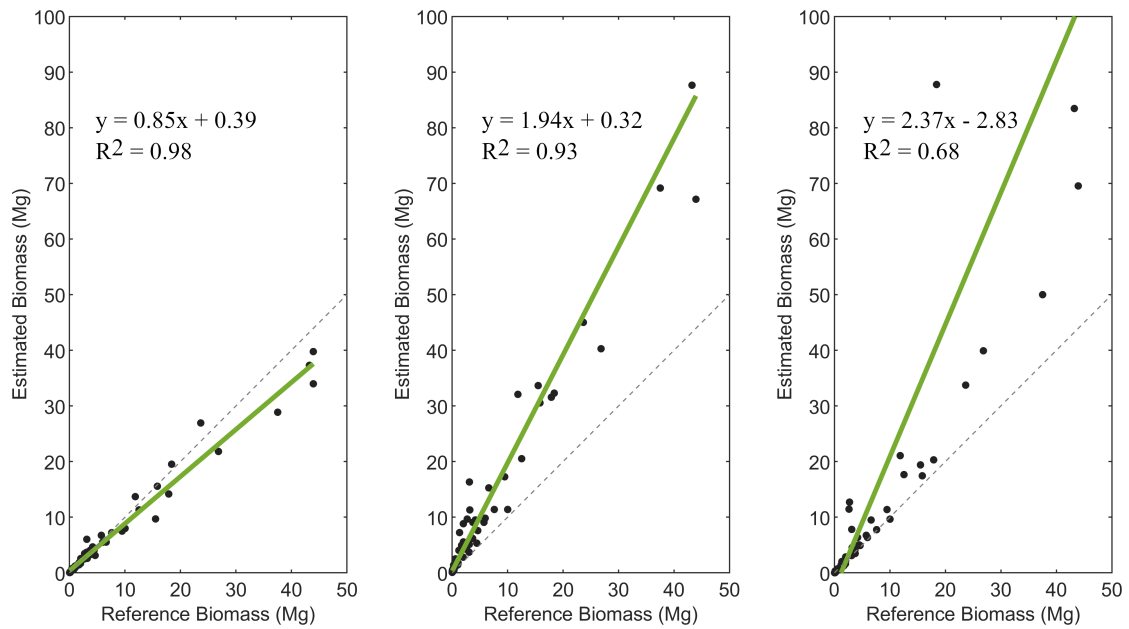


Figure 10: Left to right: Results of AGB estimation on leaf-on TLS data using our method, TreeQSM, and AdQSM.



Figure 11: Example of reconstructed 3D tree models under leaf-off and leaf-on conditions using our method.

Table 3: Results of AGB estimation on plot-scale TLS data.

| Individual Tree | MAD (Mg) | MAPD (%) |
|-----------------|----------|----------|
| Segmented | 0.23 | 19.35 |
| Reference | 0.16 | 16.69 |

reconstruction. Specifically, TreeQSM relies on cylinder fitting, which cannot effectively handle leaf points that are often misinterpreted as branches, leading to substantial overestimation. In contrast, both our method and AdQSM are graph-based approaches, where branch diameters are modeled rather than reconstructed using cylinders. As a result, they are less affected by leaf points, as also evidenced in Table 2. Notably, our method’s unique ability to control the granularity and influence of leaf points provides enhanced robustness under leaf-on conditions. The MAPD increased only slightly ($< 5\%$) compared to the leaf-off scenario.

Figure 11 further illustrates how our method robustly handled the leaf-on condition, while Figure 12 shows the reconstructed 3D tree models obtained using our method, TreeQSM, and AdQSM. These visualizations clearly demonstrate that our approach is robust under leaf-on conditions, whereas the compared methods struggle to handle leaf points effectively. For TreeQSM, this resulted in a large number of unnecessary small cylinders within the crown region, leading to significant overestimation of total AGB. In the case of AdQSM, the impact was less severe but still notable, with the MAPD increasing from 35.03% to 50.18%. Additionally, AdQSM produced an over-smoothed 3D reconstruction when compared to our method and TreeQSM, resulting in reduced visual fidelity.

5.2. Plot-scale TLS

For the plot-scale TLS data, we first present the individual tree segmentation results in Figure 13. The segmentation was performed using the method described in Section 4.2. Approximately 270 trees were segmented, while understory points were automatically identified and removed. The segmented individual trees were further reconstructed with our methods to obtain 3D models. Figure 14 presents an overview of the reconstructed 3D tree models for the RUSH06 plot. Models of the 34 reference trees were matched and used for AGB accuracy assessment.

For the matched 34 reconstructed trees, the AGB estimation

Table 4: Results of AGB estimation using ULS data with different DBH estimation methods.

| DBH Method | MAD (Mg) | MAPD (%) |
|------------|----------|----------|
| Reference | 0.06 | 3.87 |
| Estimated | 8.82 | 3237.39 |
| Allometric | 0.59 | 33.66 |

yielded a MAPD of 19.35% (Table 3). Figure 15 illustrates that our method generally underestimated AGB in this dataset, particularly for larger trees. The coefficient of determination (R^2) was 0.88. These results were obtained using fully automatic tree segmentation and reconstruction.

Since accurate tree segmentation is a critical factor in plot-scale tree reconstruction, we further evaluated the performance using reference point clouds of individual trees, thereby eliminating potential errors caused by inaccurate single tree segmentation. Under this setup, the MAPD improved to 16.69%, which is lower than that achieved by the fully automatic method. However, the difference between the two results is less than 3%, indicating that our method is relatively robust to segmentation inaccuracies. Figure 16 presents two examples of segmented trees from the RUSH06 plot and their corresponding reconstructed 3D models. We specifically selected a tree with imperfect segmentation. Nevertheless, the results shown in Table 3 and Figure 15 indicate that such segmentation imperfections had minimal impact on AGB estimation.

Moreover, for plot-scale AGB estimation, one may be interested not only in individual tree biomass but also in the cumulative AGB value across multiple trees. This is particularly useful when sampling trees to aggregate into a plot-scale AGB estimate, enabling association with large-scale AGB products. Therefore, we calculated the cumulative AGB for groups of trees, ranging from 5 to 30 trees in increments of 5. The results are shown in Figure 17. As can be seen, the accuracy of cumulative AGB remains consistent across different group sizes, with a MAPD of approximately 20%.

5.3. ULS

For the ULS dataset, since destructive AGB measurements were not available, we evaluated the relationship between ULS- and TLS-derived results. Among the 29 provided tree pairs, the fully automatic results exhibited significant bias, with an unreasonable MAPD exceeding 3000% (Table 4). This discrepancy arises because, in our method, branch diameters are *modeled* rather than *reconstructed* (Equation 1), making the initial diameter (typically DBH) a critical input parameter. For ULS data, accurate DBH estimation is particularly challenging compared to other TLS datasets. In many cases, the trunk is not clearly captured in ULS data, resulting in highly unreliable DBH estimates.

To further explore the impact of DBH estimation, we tested two alternative approaches. When using the same DBH value from TLS as input (marked as “Reference” in Table 4), the MAPD of AGB estimation was reduced to only 3.87% compared to TLS estimates (Figure 18a). This result indicates that the primary source of error originates from diameter modeling

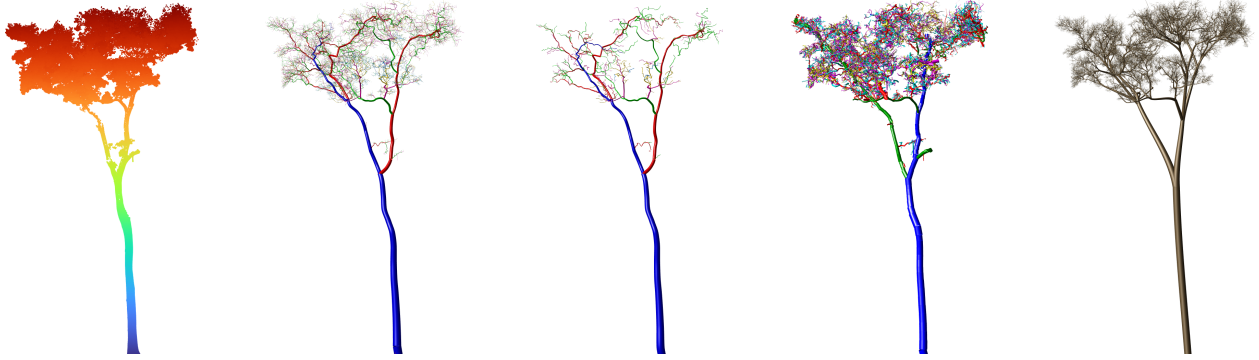


Figure 12: Comparison of reconstructed 3D tree models. From left to right: our method without path frequency control, our method with path frequency control, TreeQSM, and AdQSM.



Figure 13: Results of individual tree segmentation. Each segmented tree is colored randomly.

rather than skeleton reconstruction. A visual example is provided in Figure 19, which shows the reconstructed tree models from both TLS and ULS point clouds. The overall tree structures were reasonably reconstructed, even with heavily occluded ULS data.

The above results highlight that reliable DBH estimation is crucial for ULS data. In the absence of companion TLS data or field measurements, a practical alternative is to use allometric models to infer DBH from other structural traits that can be more reliably estimated from ULS point clouds. Tree height is strongly correlated with DBH and can be accurately estimated from ULS data. Therefore, we also tested a simple DBH–height allometric relationship to infer DBH values based on ULS-estimated tree heights. Using this allometric DBH estimation, we achieved a MAPD of 33.66% for AGB estimation with our method. Although this value is generally higher than those obtained using TLS, it remains acceptable. As shown in Figure 18c, this strategy tended to underestimate AGB overall.

6. Discussion

6.1. Graph-based 3D Tree Reconstruction: Pros and Cons

The core of our method is based on a series of graph operations. Through extensive experiments, we demonstrate that our approach exhibits strong robustness to leaf-on conditions, plot-scale data, and low-density ULS data (Table 2, 4). These

features are highly significant as they eliminate the need for pre-requisite single-tree segmentation and leaf-removal algorithms (Chen et al., 2025), and enable the application of ULS data. These advantages may facilitate much more time- and labor-efficient large-scale deployments.

As discussed in Section 2.1, current tree 3D reconstruction methods can be broadly categorized into segmentation-based and skeleton-based methods. The main difference is that the former directly fits cylinders to the point cloud without prior knowledge of the tree skeleton, while the latter first generates a skeletal structure. Fundamentally, these two paradigms reflect distinct philosophies, one emphasizes *reconstruction*, and the other *modeling*. Inherently, cylinder-fitting methods are expected to achieve higher accuracy in structural estimation, as they are fully data-driven. However, they require high-quality point clouds as input, which explains why TLS data at the single-tree level are typically preferred in such applications. Several benchmark studies have confirmed the superior performance of TreeQSM (e.g., one of the most representative cylinder-fitting methods) over graph-based alternatives (Ali et al., 2025).

On the other hand, graph-based skeleton methods, including ours, aim to capture the tree skeleton first. Since graph structures can connect nodes over long distances, they are more robust to occlusion and variations in point cloud density. As a result, the reconstructed 3D tree models are generally smoother and more complete (Chen et al., 2024). This represents a major advantage of graph-based approaches over cylinder-fitting-based methods. However, it should be noted that such smoothness and completeness do not guarantee accuracy in real tree structure. The branches reconstructed in occluded regions are purely artifacts of graph construction and may not reflect actual tree growth patterns. In most cases, these features are introduced for visual fidelity rather than structural correctness. Furthermore, branch diameters in graph-based methods are typically modeled using allometric relationships (Equation 1), which introduces two main limitations. First, the accuracy of the modeled diameters heavily depends on the universality of the adopted allometric relation, which may not be applicable across different tree species or growth conditions. Second, the initial diameter used to infer other branch diameters (usually

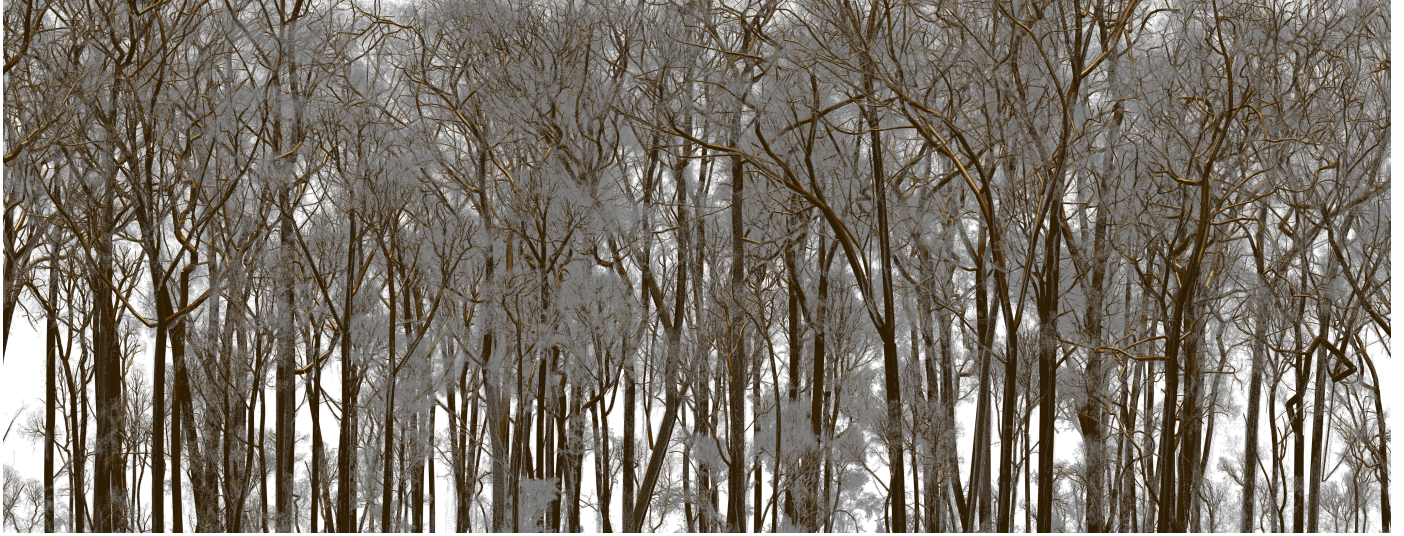


Figure 14: Close-up visualization of plot-scale tree reconstruction. Reconstructed 3D tree models are displayed together with the original point clouds (in gray), demonstrating the alignment and structural fidelity of the reconstruction approach.

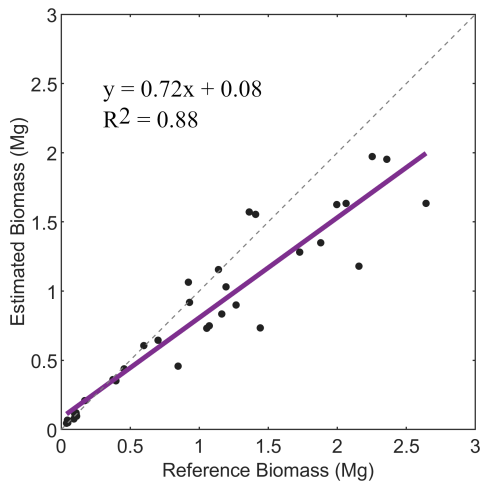


Figure 15: Results of AGB estimation on plot-scale TLS data.

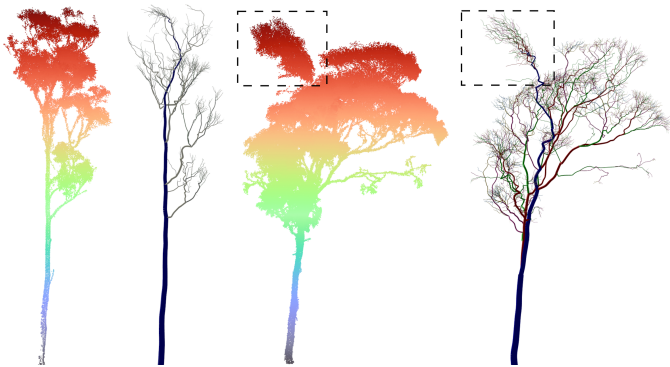


Figure 16: Examples of segmented trees and the resulting 3D reconstructions. Rectangular regions indicate locations where crown segmentation was inaccurate.

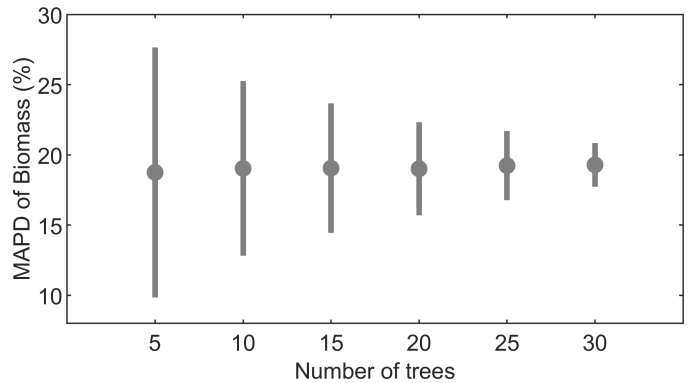


Figure 17: Cumulative AGB estimation accuracy. The dot represents the mean value, and the bar indicates the standard deviation.

DBH) is critical. If DBH is inaccurately estimated, all subsequent diameter estimates become erroneous, leading to accumulated errors in tree-level volume estimation. Our experiments on ULS data support this finding (Table 4). In contrast, cylinder-fitting-based methods estimate diameters locally from the point cloud. Even if some estimates are incorrect, they can often be corrected by neighboring segments, offering greater resilience to local errors Hackenberg et al. (2015).

Despite these limitations in volumetric and AGB estimation, graph-based methods offer significant advantages for tree 3D reconstruction. One notable advantage is that graphs provide a representation invariant to point cloud characteristics. Once converted into a graph structure, the processing pipeline remains consistent regardless of input data. In contrast, point cloud-based algorithms often require platform-specific adjustments when applied to data from TLS, ULS, or ALS. Secondly, graph-based processing generally exhibits higher computational efficiency compared to point cloud-based approaches. For instance, our method is approximately 150 times faster than TreeQSM in our experiments, while showing only a minor loss

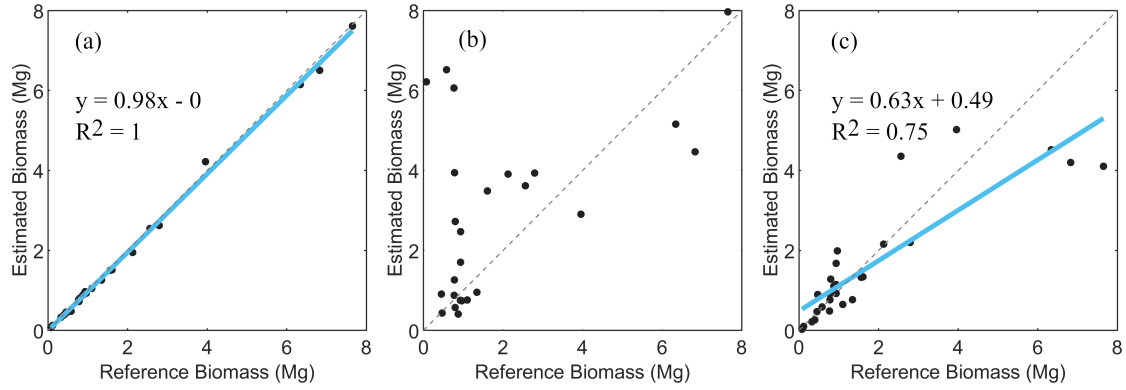


Figure 18: Results of AGB estimation using DBH values derived from (a) TLS estimates, (b) ULS estimates, and (c) an allometric model. Due to the significant bias in the ULS-based DBH estimates, linear regression was not performed for panel (b).

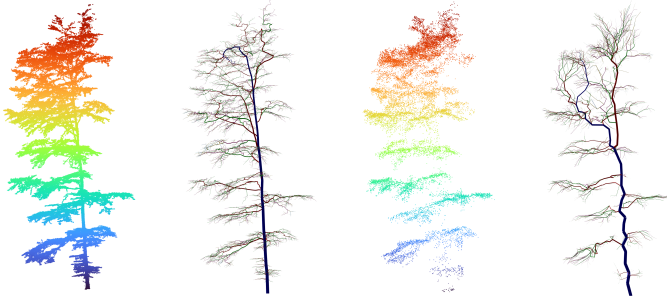


Figure 19: Comparison of 3D tree reconstruction results using TLS (left) and ULS (right) data.

in accuracy (Table 2). These results highlight the strong potential of graph-based methods for efficient and robust tree 3D reconstruction. Nonetheless, future research should focus on refining allometric modeling strategies for diameter estimation to improve the accuracy and generalizability of graph-based approaches.

6.2. Implications for Large-scale Non-Destructive Tree Biomass Estimations

Our proposed framework and the experiments provide critical insights into large-scale 3d tree reconstruction and non-destructive biomass estimation. Large-scale QSM has long been of broad interest, as single-tree-level biomass estimates are insufficient for calibrating local allometric models or serving as ground reference data for airborne or spaceborne remote sensing observations. Although previous studies Raunonen et al. (2015); Fan et al. (2022) have attempted to address this challenge, to the best of our knowledge, our approach presents the first seamless and efficient framework capable of processing large-scale point clouds directly, without decomposing the workflow into individual steps such as single tree segmentation, leaf-wood separation, and 3D reconstruction that traditionally rely on multiple algorithms and software tools. This integrated pipeline has significant implications for future large-scale QSM-based biomass estimation, offering a much more efficient and user-friendly solution.

When applied in practice, several factors should be considered. First, despite the reliable performance on plot-scale TLS data, we note that single-tree segmentation remains a major bottleneck in large-scale QSM reconstructions. As found by Martin-Ducup et al. (2021a), single-tree segmentation (particularly crown segmentation) is the primary limitation in current workflows. Our work on the RUSH06 plot, which represents a temperate forest with relatively low stem density and minimal crown overlap, yielded satisfactory results (Figure 2). However, we observed that several multi-trunk trees were not successfully segmented. This is because our graph pathing step identifies the lowest possible node as the root, and multi-trunk trees often share a common root. Therefore, in more challenging environments such as tropical rainforests, further experiments are required to evaluate the effectiveness of our approach. From the perspective of 3D tree reconstruction, it is intuitive that the completeness of a tree directly influences its overall structure and shape. Without accurate single-tree segmentation, high-quality 3D reconstruction cannot be achieved. Future research should therefore continue to focus on developing more accurate and robust single-tree segmentation methods.

On the other hand, our work demonstrates that reliable biomass estimation is still feasible using low-density and limited-coverage ULS point clouds (Table 4). Although the reconstructed tree structures may not be fully accurate (Figure 19), the overall structural integrity remains sufficient to yield reliable volume and biomass estimates. However, our experiments reveal that accurate DBH estimation from ULS point clouds is the most critical factor. This implies that, in practice, ULS data collection should be accompanied by field-measured DBH or supported by a well-calibrated allometric model capable of inferring DBH from ULS-derived structural attributes such as tree height or crown dimensions. Nonetheless, we believe that such ULS-based workflows remain significantly more time- and labor-efficient compared to acquiring large-scale TLS data. Future studies should extensively validate this ULS-based approach across diverse forest types. Additionally, understanding point cloud quality as a prior condition may be crucial for optimizing data acquisition strategies and assessing the uncertainty in QSM-based biomass estimation (Demol et al., 2022).

Currently, such knowledge is lacking.

6.3. Limitation and Future Work

Aside from the promising results on several challenging scenarios, our work also has certain limitations. First, we only tested plot-scale performance on a single dataset, and its effectiveness across different forest types and point cloud characteristics remains unknown. Conducting such comprehensive analyses requires extensive data, including large-scale point clouds, manually segmented or controlled single-tree point clouds, and their corresponding reference AGB values. Such datasets are still very rare at present, as most QSM-based AGB studies have focused on individual trees. Second, branch diameters were modeled using allometric equations (Equation 1). These equations may not be equally effective for all tree species and growth stages. The comparison in Table 2 indicates that our AGB estimation performance is inferior to TreeQSM, highlighting this limitation.

Future work should primarily focus on validating such end-to-end pipelines in more diverse environments. Very little is currently known about their generalizability, except for findings reported in Martin-Ducup et al. (2021a). Additionally, uncertainty analyses should be carried out to better understand the reliability of QSM-based biomass estimates. This is particularly important since, in practical applications, reference AGB values may not be available. An error control framework integrating point cloud quality assessment and error propagation during QSM volume estimation should be developed. In this way, QSM-based non-destructive biomass estimation can contribute more meaningfully and reliably to global forest biomass and carbon monitoring.

7. Conclusion

In this work, we propose a unified framework that integrates single-tree segmentation, leaf-wood separation, and 3D skeletal reconstruction for large-scale 3D tree reconstruction and non-destructive biomass estimation. A series of uniquely designed graph operations is introduced to enable this integrated pipeline. Extensive experiments on point clouds with varying leaf conditions (leaf-on and leaf-off), spatial scales (tree- and plot-level), and data sources (TLS and ULS) validate the effectiveness of the proposed method. Results demonstrate that our approach is robust to leaf-on conditions and low-density, partially covered ULS point clouds. Notably, the MAPD increases by less than 5% for leaf-on data compared to leaf-off conditions, without requiring separate leaf removal processing. For plot-scale data, our seamless pipeline achieved <20% MAPD at the single-tree level. Moreover, with reliable DBH estimation, biomass estimates derived from ULS data closely match those obtained from TLS. These results open up a promising new avenue for large-scale, non-destructive tree biomass estimation, as they eliminate the need for multiple dedicated tools and establish ULS data as a viable alternative. We believe this work represents a significant milestone in QSM-based tree biomass

research, paving the way for more scalable, efficient, and operationally feasible solutions for non-destructive forest biomass estimation.

References

- Ali, M., Lohani, B., Hollaus, M., Pfeifer, N., 2025. A hybrid approach for enhanced tree volume estimation of complex trees using terrestrial lidar. *GI-Science & Remote Sensing* 62, 2474836.
- Bonan, G.B., 2008. Forests and climate change: forcings, feedbacks, and the climate benefits of forests. *science* 320, 1444–1449.
- Brede, B., Terryn, L., Barbier, N., Bartholomeus, H.M., Bartolo, R., Calders, K., Derroire, G., Moorthy, S.M.K., Lau, A., Levick, S.R., et al., 2022. Non-destructive estimation of individual tree biomass: Allometric models, terrestrial and uav laser scanning. *Remote Sensing of Environment* 280, 113180.
- Burt, A., Disney, M., Calders, K., 2019. Extracting individual trees from lidar point clouds using treeseg. *Methods in Ecology and Evolution* 10, 438–445. URL: <https://besjournals.onlinelibrary.wiley.com/doi/abs/10.1111/2041-210X.13121>. doi:<https://doi.org/10.1111/2041-210X.13121>.
- Calders, K., Adams, J., Armston, J., Bartholomeus, H., Bauwens, S., Bentley, L.P., Chave, J., Danson, F.M., Demol, M., Disney, M., Gaulton, R., Krishna Moorthy, S.M., Levick, S.R., Saarinen, N., Schaaf, C., Stovall, A., Terryn, L., Wilkes, P., Verbeeck, H., 2020. Terrestrial laser scanning in forest ecology: Expanding the horizon. *Remote Sensing of Environment* 251, 112102. URL: <https://www.sciencedirect.com/science/article/pii/S003442572030475>. doi:<https://doi.org/10.1016/j.rse.2020.112102>.
- Calders, K., Newnham, G., Burt, A., Murphy, S., Raunonen, P., Herold, M., Culvenor, D., Avitabile, V., Disney, M., Armston, J., et al., 2015. Non-destructive estimates of above-ground biomass using terrestrial laser scanning. *Methods in Ecology and Evolution* 6, 198–208.
- Chen, C., Wang, H., Wang, D., Wang, D., 2024. Towards the digital twin of urban forest: 3d modeling and parameterization of large-scale urban trees from close-range laser scanning. *International Journal of Applied Earth Observation and Geoinformation* 127, 103695. URL: <https://www.sciencedirect.com/science/article/pii/S156984322400049>. doi:<https://doi.org/10.1016/j.jag.2024.103695>.
- Chen, Q., Laurin, G.V., Valentini, R., 2015. Uncertainty of remotely sensed aboveground biomass over an african tropical forest: Propagating errors from trees to plots to pixels. *Remote Sensing of Environment* 160, 134–143.
- Chen, S., Verbeeck, H., Terryn, L., Van den Broeck, W.A., Vicari, M.B., Disney, M., Origo, N., Wang, D., Xi, Z., Hopkinson, C., et al., 2025. The impact of leaf-wood separation algorithms on aboveground biomass estimation from terrestrial laser scanning. *Remote Sensing of Environment* 318, 114581.
- Comaniciu, D., Meer, P., 1999. Mean shift analysis and applications, in: *Proceedings of the seventh IEEE international conference on computer vision*, IEEE. pp. 1197–1203.
- Delagrangé, S., Jauvin, C., Rochon, P., 2014. Pypetree: A tool for reconstructing tree perennial tissues from point clouds. *Sensors* 14, 4271–4289. URL: <https://www.mdpi.com/1424-8220/14/3/4271>, doi:10.3390/s140304271.
- Demol, M., Verbeeck, H., Gielen, B., Armston, J., Burt, A., Disney, M., Duncanson, L., Hackenberg, J., Kükenbrink, D., Lau, A., et al., 2022. Estimating forest above-ground biomass with terrestrial laser scanning: Current status and future directions. *Methods in Ecology and Evolution* 13, 1628–1639.
- Du, S., Lindenbergh, R., Ledoux, H., Stoter, J., Nan, L., 2019. Adtree: Accurate, detailed, and automatic modelling of laser-scanned trees. *Remote Sensing* 11. URL: <https://www.mdpi.com/2072-4292/11/18/2074>, doi:10.3390/rs11182074.
- Duncanson, L., Armston, J., Disney, M., Avitabile, V., Barbier, N., Calders, K., Carter, S., Chave, J., Herold, M., Crowther, T.W., et al., 2019a. The importance of consistent global forest aboveground biomass product validation. *Surveys in geophysics* 40, 979–999.
- Duncanson, L., Armston, J., Disney, M., Avitabile, V., Barbier, N., Calders, K., Carter, S., Chave, J., Herold, M., Crowther, T.W., et al., 2019b. The importance of consistent global forest aboveground biomass product validation. *Surveys in geophysics* 40, 979–999.

- Duncanson, L., Armston, J., Disney, M., Avitabile, V., Barbier, N., Calders, K., Carter, S., Chave, J., Herold, M., MacBean, N., et al., 2021. Aboveground woody biomass product validation good practices protocol.
- Fan, G., Nan, L., Dong, Y., Su, X., Chen, F., 2020. Adqsm: A new method for estimating above-ground biomass from tls point clouds. *Remote Sensing* 12. URL: <https://www.mdpi.com/2072-4292/12/18/3089>, doi:10.3390/rs12183089.
- Fan, G., Xu, Z., Wang, J., Nan, L., Xiao, H., Xin, Z., Chen, F., 2022. Plot-level reconstruction of 3d tree models for aboveground biomass estimation. *Ecological Indicators* 142, 109211.
- Feng, Y., Su, Y., Wang, J., Yan, J., Qi, X., Maeda, E.E., Nunes, M.H., Zhao, X., Liu, X., Wu, X., Yang, C., Pan, J., Dong, K., Zhang, D., Hu, T., Fang, J., 2024a. L1-tree: A novel algorithm for constructing 3d tree models and estimating branch architectural traits using terrestrial laser scanning data. *Remote Sensing of Environment* 314, 114390. URL: <https://www.sciencedirect.com/science/article/pii/S0034425724004104>, doi:<https://doi.org/10.1016/j.rse.2024.114390>.
- Feng, Y., Su, Y., Wang, J., Yan, J., Qi, X., Maeda, E.E., Nunes, M.H., Zhao, X., Liu, X., Wu, X., et al., 2024b. L1-tree: A novel algorithm for constructing 3d tree models and estimating branch architectural traits using terrestrial laser scanning data. *Remote Sensing of Environment* 314, 114390.
- Fu, L., Liu, J., Zhou, J., Zhang, M., Lin, Y., 2020. Tree skeletonization for raw point cloud exploiting cylindrical shape prior. *IEEE Access* 8, 27327–27341. doi:10.1109/ACCESS.2020.2971549.
- Goetz, S.J., Baccini, A., Laporte, N.T., Johns, T., Walker, W., Kellndorfer, J., Houghton, R.A., Sun, M., 2009. Mapping and monitoring carbon stocks with satellite observations: a comparison of methods. *Carbon Balance and Management* 4, 2. URL: <https://doi.org/10.1186/1750-0680-4-2>, doi:10.1186/1750-0680-4-2.
- Hackenberg, J., Spiecker, H., Calders, K., Disney, M., Raunonen, P., 2015. Simpletree —an efficient open source tool to build tree models from tls clouds. *Forests* 6, 4245–4294. URL: <https://www.mdpi.com/1999-4907/6/11/4245>, doi:10.3390/f6114245.
- Hu, S., Li, Z., Zhang, Z., He, D., Wimmer, M., 2017. Efficient tree modeling from airborne lidar point clouds. *Computers & Graphics* 67, 1–13.
- Hyypä, J., Kelle, O., Lehtikoinen, M., Inkinen, M., 2001. A segmentation-based method to retrieve stem volume estimates from 3-d tree height models produced by laser scanners. *IEEE Transactions on Geoscience and Remote Sensing* 39, 969–975. doi:10.1109/36.921414.
- Labrière, N., Davies, S.J., Disney, M.I., Duncanson, L.I., Herold, M., Lewis, S.L., Phillips, O.L., Quegan, S., Saatchi, S.S., Schepaschenko, D.G., et al., 2023. Toward a forest biomass reference measurement system for remote sensing applications. *Global Change Biology* 29, 827–840.
- Li, J., Wu, H., Xiao, Z., Lu, H., 2022. 3d modeling of laser-scanned trees based on skeleton refined extraction. *International Journal of Applied Earth Observation and Geoinformation* 112, 102943.
- Li, Y., Su, Y., Zhao, X., Yang, M., Hu, T., Zhang, J., Liu, J., Liu, M., Guo, Q., 2020. Retrieval of tree branch architecture attributes from terrestrial laser scan data using a laplacian algorithm. *Agricultural and Forest Meteorology* 284, 107874. URL: <https://www.sciencedirect.com/science/article/pii/S0168192319304908>, doi:<https://doi.org/10.1016/j.agrformet.2019.107874>.
- Liang, X., Kankare, V., Hyypä, J., Wang, Y., Kukko, A., Haggren, H., Yu, X., Kaartinen, H., Jaakkola, A., Guan, F., Holopainen, M., Vastaranta, M., 2016. Terrestrial laser scanning in forest inventories. *ISPRS Journal of Photogrammetry and Remote Sensing* 115, 63–77. URL: <https://www.sciencedirect.com/science/article/pii/S0924271616000204>, doi:<https://doi.org/10.1016/j.isprsjprs.2016.01.006>. theme issue 'State-of-the-art in photogrammetry, remote sensing and spatial information science'.
- Martin-Ducup, O., Mofack, G., Wang, D., Raunonen, P., Ploton, P., Sonké, B., Barbier, N., Coutron, P., Pélissier, R., 2021a. Evaluation of automated pipelines for tree and plot metric estimation from tls data in tropical forest areas. *Annals of botany* 128, 753–766.
- Martin-Ducup, O., Mofack, G., Gislain, I., Wang, D., Raunonen, P., Ploton, P., Sonké, B., Barbier, N., Coutron, P., Pélissier, R., 2021b. Evaluation of automated pipelines for tree and plot metric estimation from tls data in tropical forest areas. *Annals of Botany* 128, 753–766. URL: <https://doi.org/10.1093/aob/mcab051>, doi:10.1093/aob/mcab051.
- Mei, J., Zhang, L., Wu, S., Wang, Z., Zhang, L., 2017. 3d tree modeling from incomplete point clouds via optimization and l1-mst. *International Journal of Geographical Information Science* 31, 999–1021.
- Momo Takoudjou, S., Ploton, P., Sonké, B., Hackenberg, J., Griffon, S., de Coligny, F., Kamdem, N.G., Libalah, M., Mofack, G.I., Le Moguédec, G., Pélissier, R., Barbier, N., 2018. Using terrestrial laser scanning data to estimate large tropical trees biomass and calibrate allometric models: A comparison with traditional destructive approach. *Methods in Ecology and Evolution* 9, 905–916.
- Ometto, J.P., Gorgens, E.B., de Souza Pereira, F.R., Sato, L., de Assis, M.L.R., Cantinho, R., Longo, M., Jacon, A.D., Keller, M., 2023. A biomass map of the brazilian amazon from multisource remote sensing. *Scientific Data* 10, 668.
- Raunonen, P., Casella, E., Calders, K., Murphy, S., Åkerblom, M., Kaasalainen, M., 2015. Massive-scale tree modelling from tls data. *ISPRS Annals of the Photogrammetry, Remote Sensing and Spatial Information Sciences* II-3/W4, 189–196. URL: <https://isprs-annals.copernicus.org/articles/II-3-W4/189/2015/>, doi:10.5194/isprsannals-II-3-W4-189-2015.
- Raunonen, P., Kaasalainen, M., Åkerblom, M., Kaasalainen, S., Kaartinen, H., Vastaranta, M., Holopainen, M., Disney, M., Lewis, P., 2013. Fast automatic precision tree models from terrestrial laser scanner data. *Remote Sensing* 5, 491–520. URL: <https://www.mdpi.com/2072-4292/5/2/491>, doi:10.3390/rs5020491.
- Reckziegel, R.B., Lowe, T., Devereux, T., Johnson, S.M., Rochelmeyer, E., Hutley, L.B., Doody, T., Levick, S.R., 2025. Assessing the reliability of woody vegetation structural characterisation from uav-ls in a tropical savanna. *Science of Remote Sensing* 11, 100178.
- Roxburgh, S., Paul, K., Clifford, D., England, J., Raison, R., 2015. Guidelines for constructing allometric models for the prediction of woody biomass: how many individuals to harvest? *Ecosphere* 6, 1–27.
- Gonzalez de Tanago, J., Lau, A., Bartholomeus, H., Herold, M., Avitabile, V., Raunonen, P., Martius, C., Goodman, R.C., Disney, M., Manuri, S., et al., 2018. Estimation of above-ground biomass of large tropical trees with terrestrial lidar. *Methods in Ecology and Evolution* 9, 223–234.
- Tao, S., Wu, F., Guo, Q., Wang, Y., Li, W., Xue, B., Hu, X., Li, P., Tian, D., Li, C., Yao, H., Li, Y., Xu, G., Fang, J., 2015. Segmenting tree crowns from terrestrial and mobile lidar data by exploring ecological theories. *ISPRS Journal of Photogrammetry and Remote Sensing* 110, 66–76. URL: <https://www.sciencedirect.com/science/article/pii/S0924271615002378>, doi:<https://doi.org/10.1016/j.isprsjprs.2015.10.007>.
- Terryn, L., Calders, K., Bartholomeus, H., Bartolo, R.E., Brede, B., D'hont, B., Disney, M., Herold, M., Lau, A., Shenkin, A., Whiteside, T.G., Wilkes, P., Verbeeck, H., 2022. Quantifying tropical forest structure through terrestrial and uav laser scanning fusion in australian rainforests. *Remote Sensing of Environment* 271, 112912. URL: <https://www.sciencedirect.com/science/article/pii/S0034425722000268>, doi:<https://doi.org/10.1016/j.rse.2022.112912>.
- Vandendaele, B., Martin-Ducup, O., Fournier, R.A., Pelletier, G., 2024. Evaluation of mobile laser scanning acquisition scenarios for automated wood volume estimation in a temperate hardwood forest using quantitative structural models. *Canadian Journal of Forest Research* 54, 774–792.
- Vicari, M.B., Disney, M., Wilkes, P., Burt, A., Calders, K., Woodgate, W., 2019. A tree and wood classification framework for terrestrial lidar point clouds. *Methods in Ecology and Evolution* 10, 680–694.
- Wang, D., Liang, X., Mofack, G.I., Martin-Ducup, O., 2021. Individual tree extraction from terrestrial laser scanning data via graph pathing. *Forest Ecosystems* 8, 67. URL: <https://www.sciencedirect.com/science/article/pii/S2197562023000388>, doi:<https://doi.org/10.1186/s40663-021-00340-w>.
- Wang, D., Momo Takoudjou, S., Casella, E., 2020. Lewos: A universal leaf-wood classification method to facilitate the 3d modelling of large tropical trees using terrestrial lidar. *Methods in Ecology and Evolution* 11, 376–389.
- Weiser, H., Schäfer, J., Winiwarter, L., Krašovec, N., Fassnacht, F.E., Höfle, B., 2022. Individual tree point clouds and tree measurements from multi-platform laser scanning in german forests. *Earth System Science Data* 14, 2989–3012. URL: <https://essd.copernicus.org/articles/14/2989/2022/>, doi:10.5194/essd-14-2989-2022.
- West, G.B., Brown, J.H., Enquist, B.J., 1999. A general model for the structure and allometry of plant vascular systems. *Nature* 400, 664–667.
- Wilkes, P., Disney, M., Armston, J., Bartholomeus, H., Bentley, L., Brede, B., Burt, A., Calders, K., Chavana-Bryant, C., Clewley, D., et al., 2023.

- Tls2trees: a scalable tree segmentation pipeline for tls data. *Methods in Ecology and Evolution* 14, 3083–3099.
- Wulder, M.A., White, J.C., Nelson, R.F., Næsset, E., Ørka, H.O., Coops, N.C., Hilker, T., Bater, C.W., Gobakken, T., 2012. Lidar sampling for large-area forest characterization: A review. *Remote sensing of environment* 121, 196–209.
- Ye, N., van Leeuwen, L., Nyktas, P., 2019. Analysing the potential of uav point cloud as input in quantitative structure modelling for assessment of woody biomass of single trees. *International Journal of Applied Earth Observation and Geoinformation* 81, 47–57. URL: <https://www.sciencedirect.com/science/article/pii/S030324341831225X>, doi:<https://doi.org/10.1016/j.jag.2019.05.010>.
- Zhang, W., Peng, X., Cui, G., Wang, H., Takata, D., Guo, W., 2023. Tree branch skeleton extraction from drone-based photogrammetric point cloud. *Drones* 7. URL: <https://www.mdpi.com/2504-446X/7/2/65>, doi:10.3390/drones7020065.
- Zhang, W., Qi, J., Wan, P., Wang, H., Xie, D., Wang, X., Yan, G., 2016. An easy-to-use airborne lidar data filtering method based on cloth simulation. *Remote sensing* 8, 501.